LRP 512/95 March 1995

FEASIBILITY STUDY OF THE EU HOME TEAM ON A 170GHZ 1MW CW GYROTRON FOR ECH ON ITER

C.T. Iatrou, D.R. Whaley, S. Kern, M. Thumm,
M.Q. Tran, A. Möbius, H.-U. Nickel,
P. Norajitra, A. Wien, T.M. Tran,
G. Bon Mardion, M. Pain & G. Tonon

FEASIBILITY STUDY OF THE EU HOME TEAM ON A 170GHz 1MW CW GYROTRON FOR ECH ON ITER

C. T. Iatrou[1], D. R. Whaley[3], S. Kern[1,2], M. Thumm[1,2], M. Q. Tran[3], A. Möbius[1], H.-U. Nickel[1,2], P. Norajitra[1], A. Wien[1,2], T. M. Tran[3], G. Bon Mardion[4], M. Pain[4], and G. Tonon[4]

[1]*Forschungszentrum Karlsruhe, Association EURATOM-FZK, Institut für Technische Physik, Postfach 3640, D-76021 Karlsruhe, Germany*

[2]*Universität Karlsruhe, Institut für Höchstfrequenztechnik und Elektronik, Kaiserstrasse 12, D-76128 Karlsruhe, Germany*

[3]*Centre de Recherches en Physique des Plasmas, Ecole Polytechnique Fédérale de Lausanne, Association EURATOM-Confédération Suisse, 21 Ave. des Bains, CH-1007 Lausanne, Switzerland*

[4]*Association CEA-EURATOM sur la Fusion Contrôlée, CEN-Cadarache, F-13108 Saint Paul-lez-Durance CEDEX, France*

ABSTRACT

The gyrotron system for *ECH* and burn control on *ITER* requires at least *50MW* of *RF* power at frequencies near *170GHz* operating in *CW*. To meet these requirements, high efficiency gyrotron tubes with *≥1MW* power output capability are necessary, as well as simple coupling to either a quasi-optical or waveguide transmission line. The paper reports the feasibility study on the design of an *ITER*-relevant gyrotron oscillator at *170GHz, 1MW CW* employing a diode electron gun, an advanced internal quasi-optical converter, a cryogenically cooled single disk sapphire window, and a depressed potential collector. The operating mode selection and the cavity design is a compromise between many design constraints.

Key words: gyrotron, quasi-optical converter, cryogenic window, depressed collector.

1. INTRODUCTION

The primary advantage of Electron Cyclotron Waves (ECW) as a source of auxiliary power on ITER is that EC waves can be injected into the tokamak at high power density through a simple remote launching structure with no difficulties related to plasma coupling. As a result, an ECW delivery system can be made to conform to any reactor design, including that of the shield.

The ECW system can provide startup assist together with efficient and localized heating for ITER. Heating to ignition can be achieved with *50MW* of ECW at frequencies in the range of *150-170GHz*. Current drive capability can be provided, but accompanied by increased complexity of the system. For central current drive at *6T* an increased frequency above that required for heating alone would be necessary (approx. *220GHz*). However, steady state current drive with the same heating system at *170GHz* is possible in an advanced operation scenario at *~10MA*. Other applications of ECW include $m=2$ stabilization and possibly discharge cleaning.

A single frequency system at *170GHz* could satisfy the ITER requirements of heating and current drive. The development of high power (*≥1MW*) continuous wave (*CW*) gyrotrons and windows is a critical issue to be resolved in developing an ECW system.

The present feasibility study evaluates the design of an ITER-relevant gyrotron oscillator working at *170GHz, 1MW CW* employing a cryogenically-cooled ($T=27K$) single disc sapphire window. The design constraints are shown in Table 1.

frequency, f	*170GHz±100MHz*
output power in Gaussian mode, P_{out}	*1MW*
RF efficiency, η_{rf}	*> 35%*
losses: internal Q.O. converter	*3%*
non-Gaussian output	*4%*
cryogenic window	*0.5%*
ohmic (cavity, launcher walls)	*5.5%*
cavity output power w/o losses	*1150kW*
voltage depression, $\Delta V/V_K$	*< 0.1*
cavity limiting current, I_l/I_b	*> 2*
peak wall loading, $\rho_{\Omega peak}$	*< 3kW/cm²*
sensitivity to voltage variation of *1kV* power variation, $\Delta P_{out}/P_{out}$	*< 10%*
emitter current density, j_e	*< 3.5A/cm²*
emitter over space charge current density	*< 0.2*
emitter radius, R_e	*< 50mm*
cathode electric field, E_K	*< 7.0kV/mm*

Table 1: *170GHz, 1MW CW* gyrotron design constraints.

This is a *1MW* tube operating with a total RF efficiency, including all losses up to the cryogenic window, of $\eta_{rf} = 35\%$. The peak loading of the cavity is limited to $\rho_\Omega < 3kW/cm^2$ for hot ($T = 300\,^\circ C$), non-ideal copper, corresponding to a peak loading of $\rho_\Omega < 1.5kW/cm^2$ for cold ideal copper. The cathode size is limited to a technologically feasible diameter and the current density is chosen to assure a long cathode lifetime. The electron gun is of diode type to reduce the complexity of the required high voltage power supplies and because it automatically provides a desirable α, γ beam evolution during startup. The gyrotron cavity oscillates in the $TE_{28,8}$-mode and incorporates an optimized non-linear uptaper to minimize mode conversion, followed by an advanced quasi-optical coupler allowing for a lateral output of the microwave power, and separating the electron beam from the microwave beam. A depressed collector has been designed to recuperate much of the energy of the spent electron beam. The microwave window is of cryogenic type and designed to operate at the full power of *1MW* with no risk of thermal runaway.

2. ELECTRON GUN

A diode type electron gun has been designed, using the electron beam trajectory simulation code DAPHNE [1], to produce a low-dispersion electron beam for high-efficiency cavity interaction. A large cathode provides relatively low cathode current emission density and optimized shaping of the surface opposite the emission region of the cathode creates a beam with the desired average cavity velocity pitch angle as well as low dispersion. The design allows for a low electric field on the surface of the emitter and low radial spread of the beam in the cavity. The gun has been optimized for nominal operation at $V_K = 79kV$, $I_b = 36A$, $\alpha = 1.5$. It has also however been designed such that higher values of α can be attained with equally low dispersion. The design parameters of the gun are shown in Table 2.

The magnetic field required for this gun uses the design of an existing *140GHz* cryostat currently in use at FZK which has been tested up to fields near the required field for the *170GHz* interaction ($B_0 = 6.5T$). The design magnetic field is plotted in Fig. 1. The distribution of the beam α at the location of the cavity as a function of cathode emission position is shown in Fig. 2. At the design current of $I_b = 36A$, the beam α is seen to be practically constant in the cavity ($\Delta\alpha/\alpha = 2\%$). At lower currents the beam α and dispersion increase but remain within acceptable limits. Figure 3 shows the variation of the beam α and dispersion with the applied cathode voltage. In the entire range of beam α up to $\alpha = 2.0$ and even higher a dispersion of $\Delta\alpha/\alpha \leq 5\%$ is possible. Table 2 includes the operating values necessary to produce a beam of $\alpha = 1.8$ showing that even at the elevated cathode voltages required for this α, $V_K = 85kV$, the cathode electric field remains well within acceptable limits.

average radius of emitter:	49mm
width of emitter:	3.6mm
cathode angle:	22°
cathode/anode perpendicular distance:	19.4mm
cathode voltage V_K ($\alpha = 1.5$):	79kV
cathode voltage V_K ($\alpha = 1.8$):	85kV
$\Delta\alpha/\alpha$ in cavity ($\alpha = 1.5, I_b = 36A$):	2%
$\Delta\alpha/\alpha$ in cavity ($\alpha = 1.8, I_b = 36A$):	2%
emission current density ($I_b = 36A$) j_e:	3.0A/cm^2
beam radius in cavity:	8.4mm
r_{beam}/r_{cavity}:	0.50
$\Delta r_{beam}/r_{beam}$ in cavity:	2%
beam depression in cavity ($\alpha = 1.5$):	5.6kV
optimum cathode magnetic field gradient:	0.17T/mm
maximum cathode electric field ($\alpha = 1.5$):	5.1kV/cm
maximum cathode electric field ($\alpha = 1.8$):	5.4kV/cm
cavity magnetic field:	6.67T
cavity magnetic field gradient:	0.0G/mm
beam compression	32.5

Table 2: Gun design parameters.

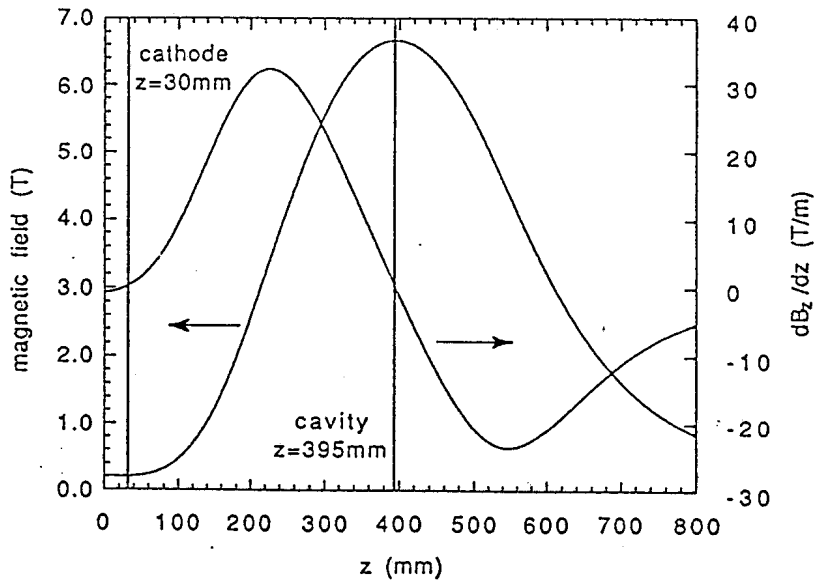

Fig. 1: Axial magnetic field profile.

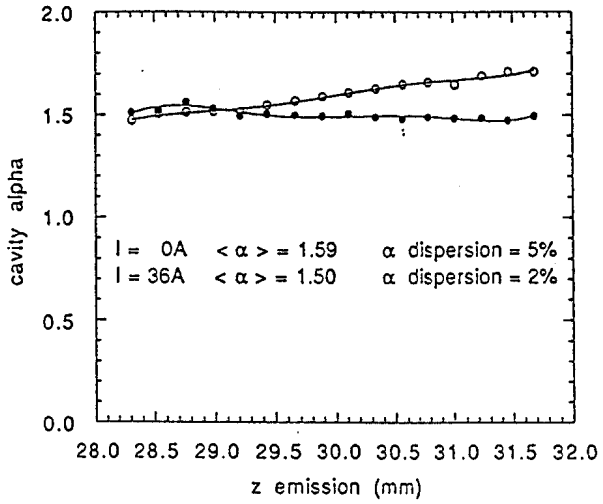

Fig. 2: Electron velocity ratio distribution in cavity.

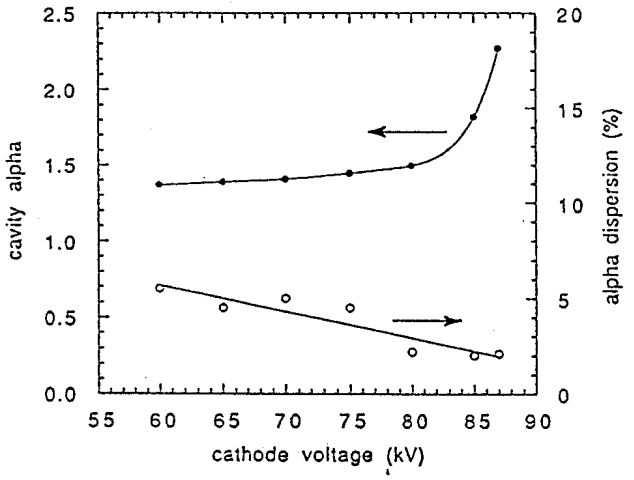

Fig. 3 : Electron velocity ratio and dispersion dependence on cathode voltage.

3. DEPRESSED COLLECTOR

Use of depressed collectors is a method for improving the system efficiency of electron tubes by partially recovering the energy of the spent electron beam [2,3,4]. A depressed collector is incorporated into the design of the *170GHz* gyrotron. It is isolated from the grounded body of the gyrotron and the electron beam is collected at a potential intermediate between that of the cathode potential and that of the grounded body. For an arbitrary electron distribution, $f(E)$, the collector recovery efficiency is defined as:

$$\eta_c(\phi_c) = 1 - \frac{\int_{q_e\phi_c}^{E_{max}} f(E)(E - q_e\phi_c)dE}{\int_{q_e\phi_c}^{E_{max}} f(E)EdE} = \frac{q_e\phi_c}{\overline{E}} \qquad (1)$$

where η_c is the collector recovery efficiency, $f(E)$ is the electron energy distribution at the input of the collector region, ϕ_c is the collector potential, $\overline{E}$ is the average energy of the distribution, E_{max} is the maximum energy of particles in the distribution.

The effect of the cavity interaction on the beam energy distribution and subsequently on the recovery efficiency are presented in Figs. 4 and 5. A monoenergetic beam with a dispersion in perpendicular momentum of $\Delta p_\perp/p_\perp = 10\%$ is considered. After cavity interaction with the $TE_{28,8}$-mode, the distribution function appears as shown in Figs. 4(c) and (d). Here it is seen that the majority of the distribution has been shifted to low energy of about $35kV$ with a tail to the high energy side. The main part of the distribution is very close to the minimum energy located at $30kV$. This will allow for efficient recovery of the beam as the collector can be biased at a potential near this minimum energy. A distribution of particles representative of the distribution shown in Fig. 4(d) is then reinjected into the particle simulation at the location of the end of the cavity and propagated to the depressed collector. The recovery efficiency as a function of collector potential for the distribution of Fig. 4 is shown in Fig. 5.

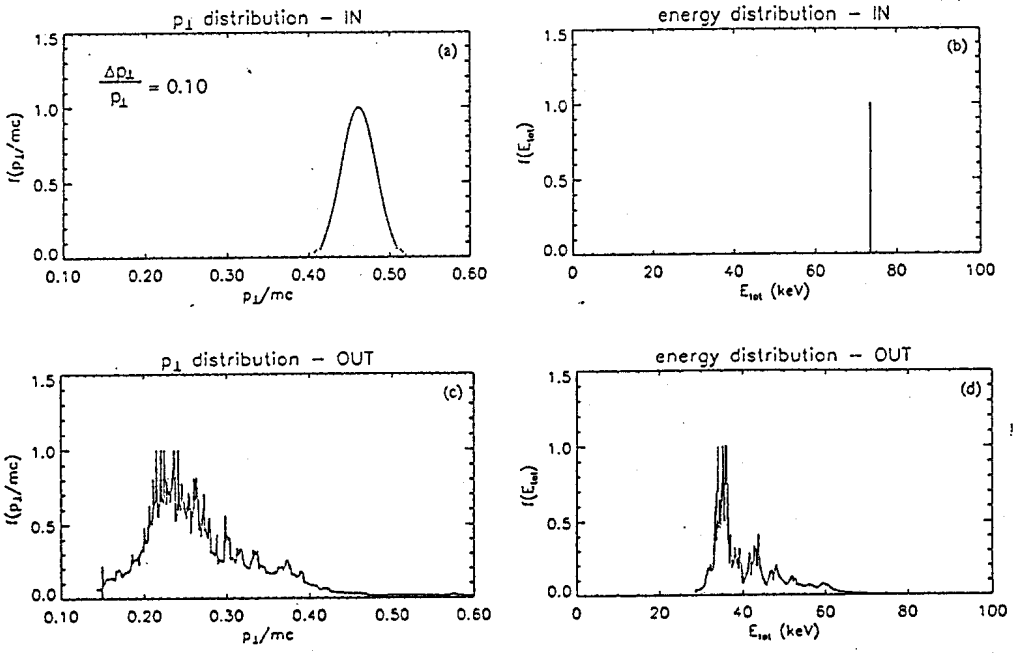

Fig. 4: (a) (b) initial perpendicular momentum and energy distribution of beam before interaction for $\Delta p_\perp/p_\perp = 0.10$ (c) (d) perpendicular momentum and energy distribution of beam after interaction.

The recovery efficiency is plotted up to a collector potential corresponding to the minimum energy of the distribution. In this case, the maximum recovery efficiency is seen to be $\eta_c = \sim 65\%$. The collector to ground potential is set to $\phi_c = -27kV$. The collector cannot be biased at voltages much below the value of $\phi_c = -27kV$ or reflection of part of the beam will result.

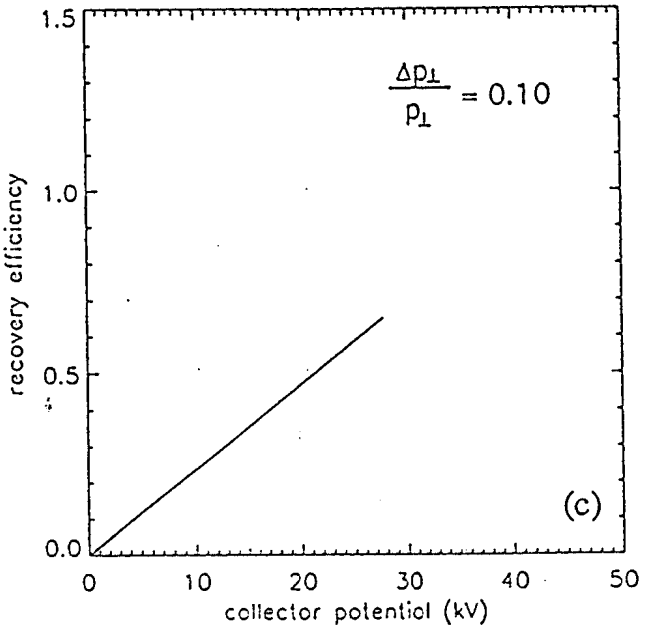

Fig. 5: Collector recovery efficiency vs. collector potential for an electron beam with initial momentum spread $\Delta p_\perp / p_\perp = 0.10$.

Up to this point, the depressed collector that has been discussed is comprised of one stage. That is that the entire distribution of the electron beam is decelerated to the same potential - that of the one-stage collector. It may be possible to separate the electron beam - collecting the lower energy part of the distribution on the first stage of a two stage collector and the remaining part of the distribution on the second stage. This would increase the recovery efficiency over that of a one-stage depressed collector. This increase in recovery efficiency may be calculated using the distribution of Fig. 4(d). If one assumes a two-stage depressed collector, separating the distribution of Fig. 4(d) into a distribution below $E_{tot} = 40keV$ and a distribution above $E_{tot} = 40keV$, the resulting recovery efficiency can be calculated as:

$$\eta_c = f_1 \frac{q_e \phi_{c1}}{\overline{E_1}} + f_2 \frac{q_e \phi_{c2}}{\overline{E_2}} \qquad (2)$$

where f_1 is the fraction of the distribution lying in the energy range

$0 < E < 40keV$ and f_2 is the fraction of the distribution lying in the energy range $40keV < E < E_{max}$. The recovery efficiency for a two stage collector with the distribution of Fig. 4(d) can be shown to increase to $\eta_c = \sim 76\%$.

The total system efficiency is then defined as:

$$\eta_{sys} = \frac{P_{out}}{P_{b0} - P_{rec}} = \frac{\eta_{rf} P_{b0}}{P_{b0} - \eta_c P_b} = \frac{\eta_{rf}}{1 - \eta_c (1 - \eta_{rf})} \qquad (3)$$

where η_{rf} is the rf efficiency, P_{out} is the microwave power, P_{b0} is the initial beam power, P_b is the spent beam power after interaction and $P_{rec} = \eta_c P_b$ is the recovered beam power. Plots of total system efficiency as a function of recovery efficiency for several values of RF efficiency is shown in Fig. 6. If one assumes a RF efficiency of $\eta_{rf} = 36\%$ as is shown in Sec. 4, a single-stage collector with $\Delta p_\perp / p_\perp = 0$ results in a system efficiency of $\eta_{sys} = 0.70$. Once dispersion is added to the cavity input beam, the attainable system efficiency decreases to $\eta_{sys} = 0.65$. This could possibly be recovered by adding a second stage to the depressed collector which would again increase the system efficiency to $\eta_{sys} = 0.70$. This though would be at the expense of a more complex design of the internal collector structure as well as the added risk of reflected electrons. A two-stage collector would also preclude the use of a collector sweeping coil to decrease the power loading by spreading the spent beam on the interior of the collector.

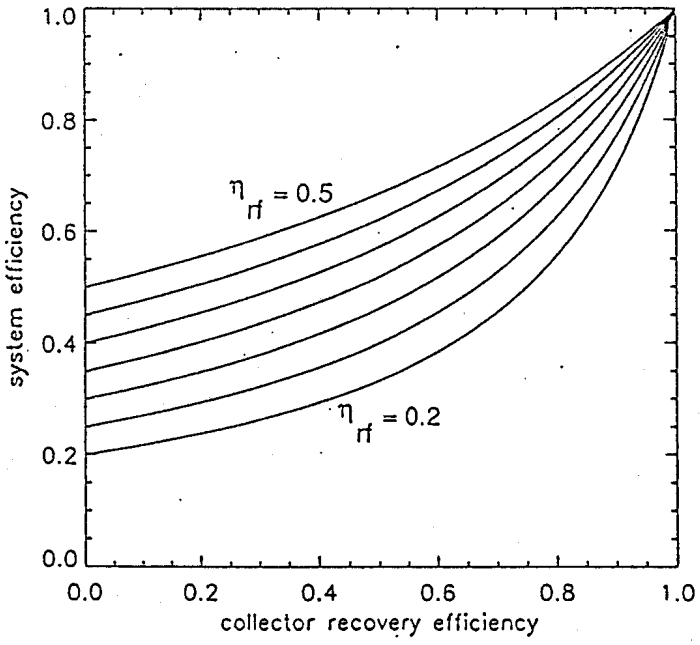

Fig. 6: System efficiency vs. collector recovery efficiency for several values of RF efficiency η_{rf}.

4. CAVITY DESIGN AND INTERACTION CALCULATIONS

4.1 Mode Selection

The procedure for the selection of the operating mode and the determination of the general design parameters for the *170GHz* gyrotron cavity is based on the method of normalized variables [5,6]. According to this method, the beam/RF interaction in the gyrotron cavity can be fully described by three normalized variables, namely the electric field strength F, the interaction length μ, and the detuning parameter Δ:

$$F = \frac{E_0}{B_0 \beta_\perp^3 c} J_{m\pm1}(k_\perp R_b) \tag{4a}$$

$$\mu = \pi \frac{\beta_\perp^2}{\beta_{//}} \frac{L}{\lambda} \tag{4b}$$

$$\Delta = \frac{2}{\beta_\perp^2}(1 - \frac{\omega_c}{\omega}) \tag{4c}$$

where E_0 is the intensity of the RF electric field, B_0 is the induction of the static magnetic field, ω_c is the relativistic electron cyclotron frequency, ω is the wave frequency, λ is the free-space wavelength, R_b the beam radius, $\beta_\perp$ and $\beta_{//}$ the perpendicular and parallel electron velocities normalized to the speed of light c, $k_\perp = \chi_{mp}/R_0$ is the perpendicular wavenumber, χ_{mp} is the p^{th} root of $J'_m(x) = 0$, R_0 the cavity radius, and L is the *1/e* length of the assumed Gaussian axial profile of the electric field. The $\pm$ signs of the Bessel functions refer to the rotation of the electric field relative to the electron motion. The minus sign corresponds to a field that rotates in the same sense as the electrons.

Assuming a realistic electron velocity ratio of $\alpha = \beta_\perp/\beta_{//} = 1.5$, a perpendicular efficiency of $\eta_\perp \sim 65\%$ is required for an acceptable electronic efficiency near $\eta_{elec} \sim 45\%$. A compromise is made between the cavity length and corresponding required electric field to achieve the desired interaction efficiency. A long cavity is able to reach the desired efficiency with a low electric field, which is preferable for wall loading, but in general it makes the cavity highly sensitive to even a small percentage of reflected power, increases the risk of oscillation in higher axial harmonics and precludes high-efficiency operation of the cavity in the soft-excitation region. These considerations lead to an operating point of:

$$F=0.1 \qquad \mu=16 \qquad \Delta_{opt}=0.46 \tag{5}$$

The peak cavity wall loading can be calculated as:

$$\rho_{\Omega\,peak} = 1.67 \times 5.1 \times 10^{-15} \sigma^{-1/2} \omega^{5/2} \beta_{\perp}^{6} \gamma^{2} F^{2} C_{mp}^{2} (1 - 0.5\beta_{\perp}^{2})^{2} \qquad (6)$$

where $C_{mp} = J_m(\chi_{mp})/J_{m-1}(\chi_{mp} R_b/R_0)$, and the factor 1.67 is the peak-to-average Gaussian squared factor. Though, as seen above, a low beam voltage leads to lower wall loading, it might prove problematic due to the associated voltage depression and limiting current, as well as the emitter current density through the increased beam current required to achieve high output power. For a beam voltage V_b, the voltage depression ΔV due to space charge of the beam is computed by the formula:

$$\Delta V = \frac{30 G I_b}{\beta_{//}} \qquad (7)$$

where the factor G is given by:

$$G = \frac{3}{4} \frac{\Delta_b}{R_b} + 2 \ln \frac{R_0}{R_b + \frac{\Delta_b}{2}} \qquad (8)$$

and Δ_b is the total beam thickness in the cavity, usually taken equal to four Larmor radii. The beam current is computed from the required output power, the total efficiency and the cathode voltage V_K:

$$I_b = \frac{P_{out}}{\eta_{rf} V_K} \qquad (9)$$

As can be seen by Eq. (7), increasing the beam current increases the voltage depression and a large current will approach the limit where steady-state current flow is no longer possible. This limiting current is given by:

$$I_L = 1.707 \times 10^{4} \gamma_0 [1 - (1 - \beta_{//0}^{2})^{1/3}]^{3/2} G^{-1} \qquad (10)$$

where γ_0 and $\beta_{//0}$ refer to the corresponding beam γ and $\beta_{//}$ without potential depression.

An acceptable mode for operation of the *170GHz* gyrotron, fulfilling all constraints listed in Table 1, is now defined. Modes with $2 \leq m \leq 40$ and $2 \leq p \leq 12$, where m = *azimuthal index* and p = *radial index* are considered. Figure 7(a) shows the peak wall loading as a function of the mode eigenvalue. The beam voltage is assumed *73kV*, the beam current for each mode is determined as that necessary to provide an output window power of *1MW*, and the beam is assumed to be placed at the innermost peak of the electric field of each mode, with the polarization chosen as that which rotates in the same sense as the electrons. The choice of beam

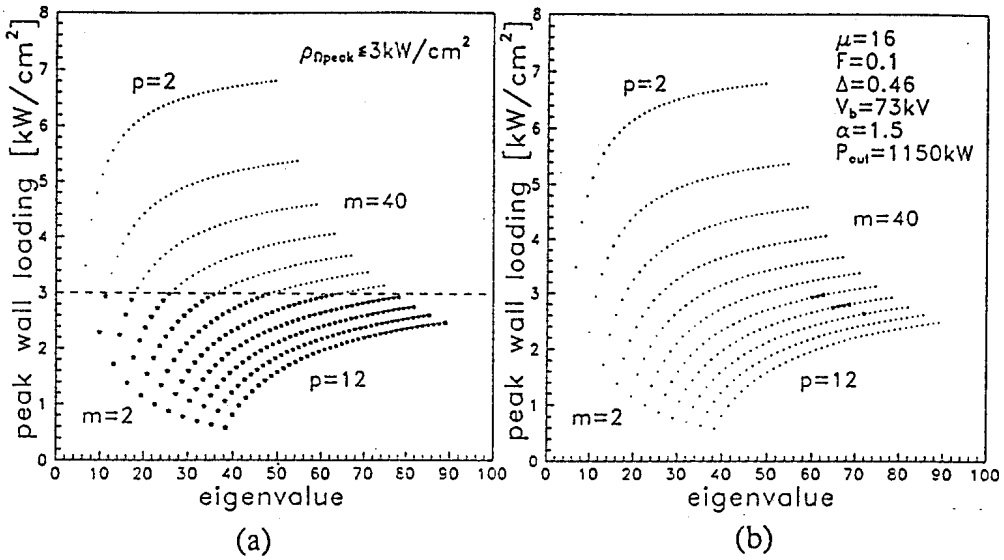

Fig. 7: Peak wall loading vs. mode eigenvalue for all modes with $2 \leq m \leq 40$ and $2 \leq p \leq 12$ (a) modes satisfying the wall loading constraint of $\rho_\Omega \leq 3kW/cm^2$ (solid stars) (b) modes satisfying all design constraints of Table 1 (solid stars).

voltage of $73kV$ in the cavity will be discussed later. The wall loading is computed for hot Glidcop - corresponding to an ohmic loading two times that of the ideal copper. The magnetic compression is limited between 25 and 40, which can change with the mode, and the beam thickness in the cavity is assumed at $\Delta_b = 4r_L$. The dependence of wall loading on the choice of azimuthal and radial mode number is easily seen in Fig. 7(a). Increasing the azimuthal mode number for a constant radial mode increases the loading, while increasing the radial mode number decreases the loading. Modes which allow for a wall loading of $\rho_{\Omega peak} < 3.0kW/cm^2$ are readily identifiable and are marked with a solid star in the figure. In Fig. 7(b) indicated in bold are the modes which fulfill all the design constraints for parameters listed in Table 1. As seen, there are several modes which meet all criteria. In general, the upper cutoff of Fig. 7(b) is a result of the constraint on cathode size of $R_E < 50mm$ and the lower cutoff is a result of the constraint on cathode current density of $j_e < 3.5A/cm^2$. The beam voltage of $V_b = 73kV$ was chosen as that in a generally acceptable range of $70kV < V_b < 75kV$ for the $p = 8$ radial mode series. The $p = 7$ radial mode series corresponds to lower beam voltages (68-74kV) and are of particular interest since, in general, they suffer less from azimuthal mode competition. However, modes with radial index 7 are not considered as possible working modes because in the particular range of azimuthal mode numbers of interest, they are very close in frequency to the main competing modes, those which couple well to the beam. Allowing for a radial mode series at or above the $p = 8$ series, an optimum beam

voltage of V_b =*70-75kV* has been determined from loading considerations. Figure 7(b) shows that the mode in the $p = 8$ radial mode series with the lowest azimuthal mode number is the $TE_{28,8}$-. This is the choice for the operating mode of the *170GHz* cavity as it satisfies all design criteria and has reasonably good frequency separation (*622MHz*) with its main competitor $TE_{25,9+}$ and *3.5GHz* from the neighboring azimuthal modes.

The Q value for a cavity can be calculated as:

$$Q = \frac{4.31\times 10^6}{\pi}\,\frac{\alpha\beta_{//}^2\beta_{\perp}^3\gamma^2F^2(\chi_{mp}^2-m^2)(1-0.5\beta_{\perp}^2\Delta)^2}{P_{out}} \qquad (11)$$

and is used as a guide for the design of the required $TE_{28,8}$- cavity presented in the following section.

4.2 Beam/RF Interaction and Design Values

The cavity shown in Fig. 8 is designed to oscillate in the $TE_{28,8}$- mode at *170GHz*, with an equivalent Gaussian length and a diffractive quality-factor Q_0 close to that computed by the normalized variable method. The angles joining the different sections of the cavity are smoothed with a parabolic smoothing length of *4mm* to minimize mode conversion. The choice of *3.5°* for the input angle minimizes the risk of oscillation of competing modes in the downtaper section and quickly forms a cutoff section for modes near the $TE_{28,8}$- to keep power transmission to the gun to a minimum. The actual uptaper profile is non-linear, formed to minimize mode conversion after this section of rapidly changing radius and to provide the shortest distance between the cavity output and the quasi-optical launcher. The mode purity of power exiting the non-linear uptaper is calculated to be *99.8%*. The linear uptaper presented in Fig. 8 is used only for numerical simulations and its angle is choosen so that a coupling factor between beam and RF as close as possible to the one of the non-linear uptaper is provided.

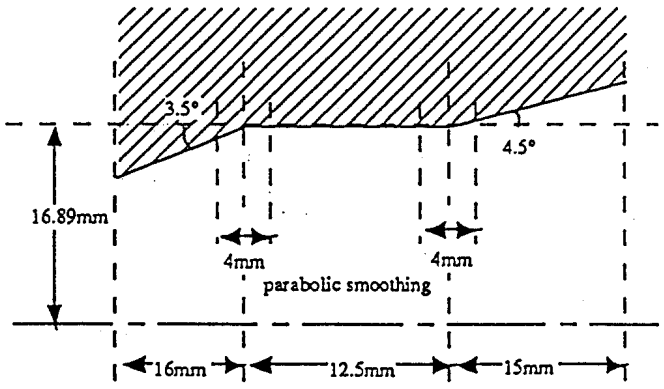

Fig. 8: *170GHz/$TE_{28,8}$* cavity geometry. All length dimensions in *mm*.

To determine the precise design values which will yield the optimum performance of the tube, the beam/RF interaction is computed self-consistently with the actual field profile [7]. A numerical code integrates the equations of electron motion along the cavity, for an ensemble of electrons uniformly distributed in azimuth, self-consistently with Maxwell's equations, computing the energy exchange between the electron beam and the electromagnetic field of the cavity. The solution is determined by imposing a cutoff condition at the input of the cavity and a traveling wave condition at the output. Thus the actual field profile is determined and the electronic efficiency is computed as:

$$\eta_{\text{elec}} = \frac{\gamma_{\text{in}} - \langle \gamma_{\text{out}} \rangle}{\gamma_{\text{in}} - 1} \tag{12}$$

where γ_{in} is the initial value of the relativistic mass factor, equal for all particles, and $<\gamma_{out}>$ is the average of γ over all particles leaving the interaction space. An RF efficiency is also computed by integrating the Poynting vector over the output cross-section of the cavity, after the field amplitude and the resonant frequency have been computed from the solution of Maxwell and electron-motion equations. These two efficiencies must be practically equal.

The maximum coupling between the beam and the operating mode $TE_{28,8}$- is obtained by placing the beam at a radius of *8.29mm*. In order to decrease the coupling to the $TE_{25,9}$+, which is very close in frequency to $TE_{28,8}$- and may cause mode competition problems, the beam radius is increased to *8.40mm*. The relative coupling coefficient of $TE_{25,9}$+ is reduced from *0.97* to *0.71* while that of the $TE_{28,8}$- remains practically unchanged.

The operating point is chosen in Figs. 9. Here, the results of the self-consistent code are presented for a constant output power of P_{out} = *1MW*, computed for several beam energies from *69keV* to *75keV*. Figure 9(a) shows the required beam current to achieve a *1MW* output power and the corresponding RF efficiency. Voltage depression due to beam space charge is taken into account in the calculation of RF efficiency. The peak cavity wall loading and the ratio of the limiting current to the beam current are presented in Figs. 9(b) and (c) respectively. Higher efficiency is seen to be obtained using low energy beams. The limit of *35%* total efficiency is barely achieved at a magnetic field of *6.69T* for a beam energy of *75keV*. Moreover, as can be seen from Fig. 9(b), high energy beams will strongly load the cavity walls. On the other hand, a low energy beam requires a high beam current to yield *1MW* output power, and thus for a *69keV* energy beam the limiting current is less than twice the beam current in the whole range of magnetic field. The useful range for beam energy is therefore limited between *71keV* and *75keV*, with corresponding magnetic field range from *6.63T* to *6.69T*. Selecting a cathode voltage of *79kV* and a beam current of *36A*, a beam energy of *73.4keV* is computed

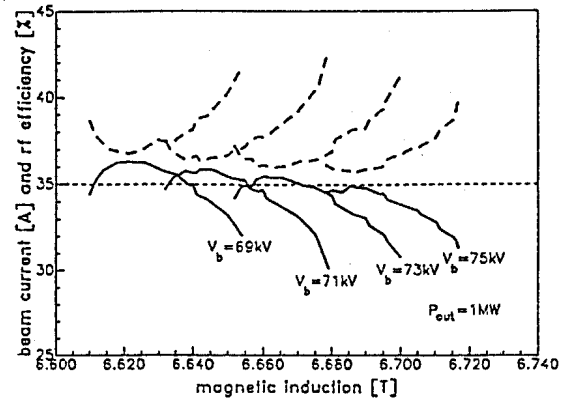

(a)

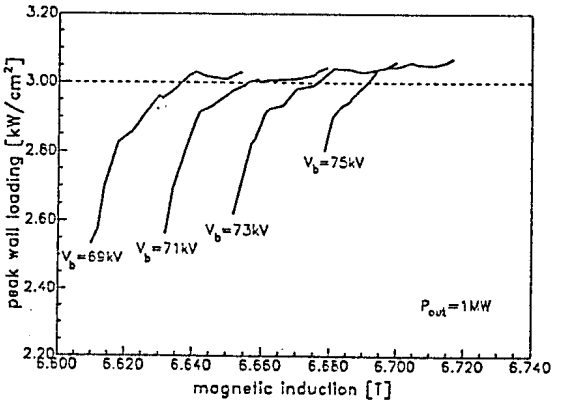

(b)

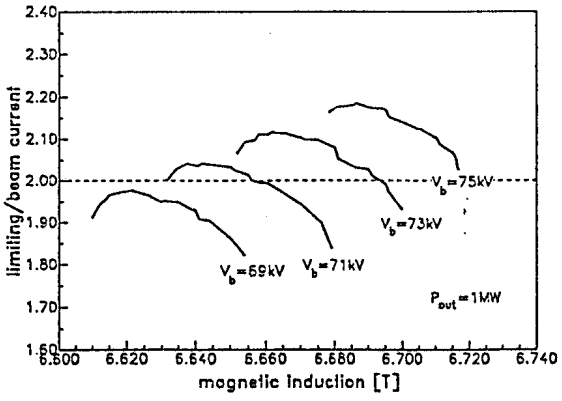

(c)

Fig. 9: (a) required beam current and RF efficiency (b) realistic peak wall loading (c) limiting-to-beam current ratio vs. magnetic field for constant output power *1MW* and several values for beam voltage V_b.

after voltage depression with electron velocity ratio of its design value of $\alpha = 1.5$ inside the cavity. The design magnetic field becomes $B_0 = 6.67T$ and the $TE_{28,8}$- mode oscillates at a frequency of $f = 170.004GHz$ with an electronic efficiency of $\eta_{elec} = 44\%$. The peak wall-loading is computed to $2.97kW/cm^2$, and the power dissipated in the cavity walls is $34kW$. Assuming $\sim 10\%$ RF losses after the cavity (see Table 1), an output power in the Gaussian beam of $1016kW$ and an RF efficiency of 35.7% are computed. The limiting current at the operating point is $77A$ and the loaded quality factor is 1185, in very good agreement with the predictions of the normalized variable method. These $170GHz$ design values are summarized in Table 3.

The behavior of the proposed cavity with respect to variations in several operating parameters is now presented. The response of the cavity to magnetic field variation is shown in Fig. 10. Here, the electronic and RF efficiency is given as a function of magnetic field, at the operating cathode voltage of $79kV$ and beam current of $36A$. The border between hard and soft excitation regions is seen to occur at a magnetic field of $6.702T$, and the corresponding RF efficiency drops to 32% with an output power of $910kW$. Although the drop of power and efficiency is not dramatic, it is necessary to enter the hard excitation region to reach high-efficiency, high-power operating conditions. In a CW tube, one can manually move from the soft- to the hard-excitation region by varying the magnetic field on a slow time scale. A diode startup also allows access to the hard-excitation region as both the beam γ and α increase together during the cathode voltage rampup. This allows for single mode excitation of the $TE_{28,8}$- which remains stable up to the operating cathode voltage of $79kV$, suppressing all possible competitors.

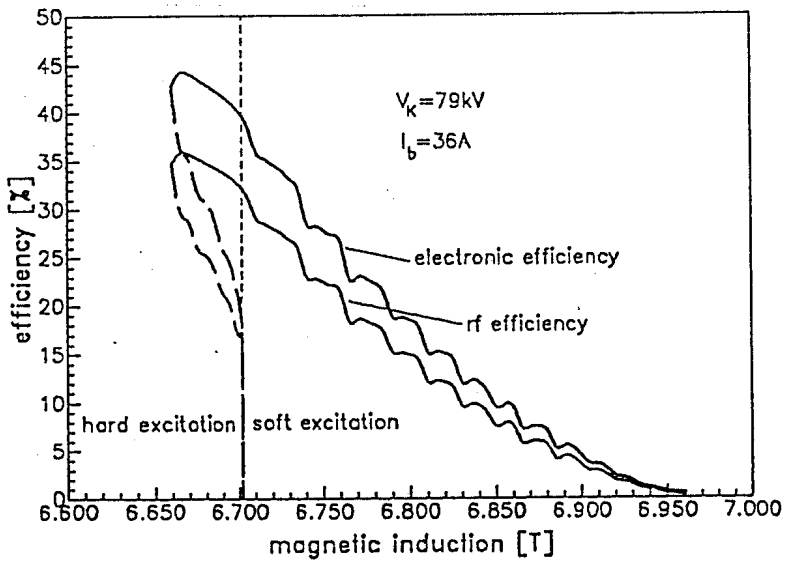

Fig. 10: Electronic and RF efficiency vs. magnetic field at cathode voltage $V_K = 79kV$ and beam current $I_b = 36A$.

operating mode	$TE_{28,8}$-
frequency, f	170.004GHz
RF efficiency, η_{rf}	35.7%
magnetic field, B_0	6.67T
cathode voltage, V_K	79kV
beam current, I_b	36A
voltage depression, ΔV	5.6kV
beam energy, E_{beam}	73.4keV
cavity output power w/o losses	1164kW
electronic efficiency, η_{elec}	44%
peak wall loading, $\rho_{\Omega, peak}$	2.97kW/cm²
total cavity wall losses	34kW
diffractive quality factor, Q_0	1220
ohmic quality factor, Q_{ohm}	41555
total quality factor, Q_T	1185
limiting current, I_L	77A
normalized Gaussian length, μ	15
sensitivity to voltage variation $\Delta V_K = 1kV$ frequency variation, Δf power variation, $\Delta P/P$	 6MHz 6.9%

Table 3: Beam and cavity parameters for 170GHz 1MW CW gyrotron.

The design criteria regarding cathode voltage variation, in practice due to power supply ripple, are also seen to be fulfilled in Table 3. A variation of $1kV$ in V_K results in a decrease in the output power of less than 7% and a decrease in the RF efficiency by less than 2%, well inside the design limit.

Sensitivity of the interaction to transverse electron velocity spread is also considered. An effective velocity spread of 10% results in a decrease of the output power by 8% to $935kW$ with a corresponding total RF efficiency of 32.9%.

4.3 Mode Competition and Startup

The mode spectrum near the $TE_{28,8}$- mode is dense and many of the nearby modes couple well to the electron beam. Since the quality factors of these modes are not significantly different from that of the $TE_{28,8}$- mode, the starting current requirements will be practically the same for a number of modes, and thus careful consideration must be given to mode

competition to assure a monomode operation in the designed operating mode.

To determine which modes might be competitors with the $TE_{28,8}$- mode, starting current curves have been generated using a self-consistent code and they are presented in Fig. 11. The beam parameters are treated as functions of the cathode voltage, with the beam α assumed to change with the cathode voltage according to Fig. 3. The beam current also plotted in Fig. 11 as a function of the cathode voltage, is computed using the formula $I_b = I_0 exp(0.786 E_{K0}^{1/2}((V_K/V_{K0})^{1/2}-1))$, where I_0 and V_{K0} are the final values of the beam current and the cathode voltage at the operating point and E_{K0} is the average electric field at the surface of the cathode at the operating point. The magnetic field is fixed at the design value of $B_0 = 6.67T$. According to this figure the first mode to be excited is the $TE_{29,8}$- as the cathode voltage reaches the value of $43kV$.

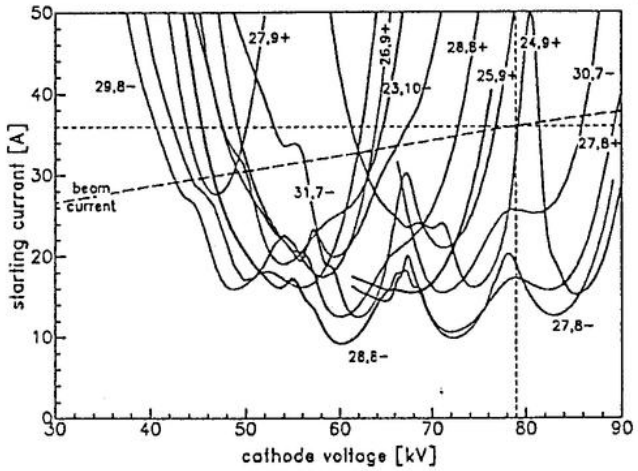

Fig. 11: Self-consistent starting current vs. cathode voltage at $B_0 = 6.67T$.

To determine whether the $TE_{28,8}$- will exhibit stable oscillations during startup and at the operating point, the entire startup of the tube has been simulated and is shown in Fig. 12. A fixed-field mode competition code [8] has been used to determine the mode stability against all competing modes. To account for beam loading effects, the single-mode self-consistent code is first used to provide the mode field profile at any cathode voltage, and this profile is then used in the mode competition computations for stability analysis. The figure shows the linear rampup of the cathode voltage. The $TE_{29,8}$- mode is the first exited mode during the startup, oscillating at voltages as low as $V_K = 43kV$. As the cathode voltage increases during the startup, the $TE_{28,8}$- replaces the $TE_{29,8}$- at $V_K = 65kV$. The $TE_{28,8}$- then remains the stable operating mode up to the operating point at $V_K = 79kV, I_b = 36A$, suppressing all competitors. All of the modes of Fig. 11 with starting current less than $I_b = 36A$ have been checked concerning their competing influence on the stability of the $TE_{28,8}$- mode during startup.

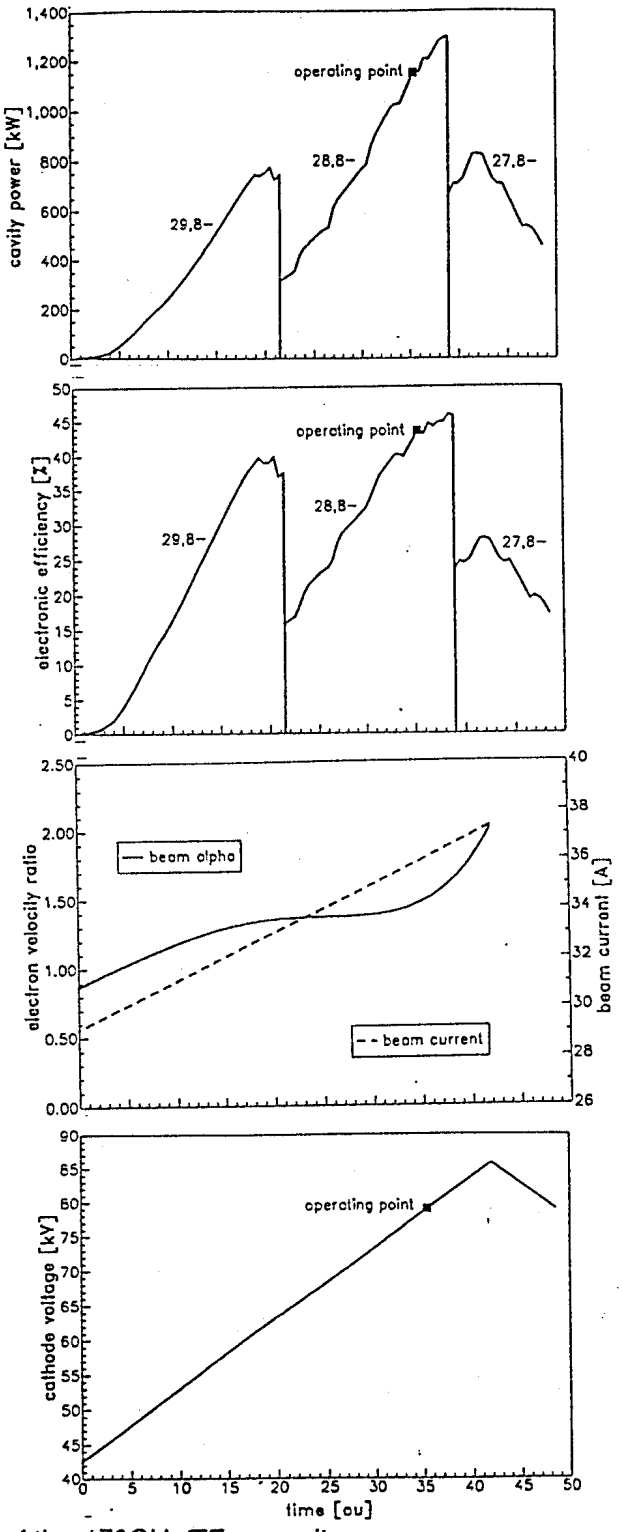

Fig. 12: Startup of the *170GHz/TE$_{28,8}$* cavity.

To simulate the effect of power supply overshooting, the cathode voltage is further increased during the startup simulations to the point where the operating mode ceases oscillation allowing for another mode, the one with the minimum starting current at the beam conditions, to start to oscillate. This was found to occur at a cathode voltage of $V_K = 83kV - 4kV$ above the operating voltage. At this point the operating mode $TE_{28,8}$- does not cease oscillating because of mode competition of $TE_{27,8}$-, but rather it reaches a point where the beam parameters do not allow oscillation of this mode at any power. Once the parasitic mode $TE_{27,8}$- has been established, even if the beam parameters return to their nominal design values after the overshoot, as is the case in Fig. 12, the cavity is seen to continue oscillating in the parasitic mode $TE_{27,8}$-, with lower efficiency and output power. Oscillation does not return to nominal values and therefore care must be taken not to overshoot the operating point by more than a safe limit of ~2.5%, to assure monomode operation at the operating point in the desired mode $TE_{28,8}$-.

5. QUASI-OPTICAL MODE CONVERTER

Radial output coupling of the RF power of a gyrotron into a Gaussian ($TEM_{0,0}$) mode has three significant advantages for high-power operation. First, the linearly polarized $TEM_{0,0}$ mode is directly usable for low-loss transmission as well as for effective interaction with the fusion plasma and no further mode converters are needed. Second, the converter separates the electron beam from the RF wave path, so that the electron collector is no longer part of the output waveguide as in the case of a tube with an axial output. Hence, the collector can be designed especially for handling the high electron beam power. In addition, energy recovery with a depressed collector becomes possible. Third, the influence of RF power reflected from the output window and the load is expected to be significantly reduced especially for modes rotating in the opposite direction from the design mode.

As in most advanced gyrotrons with lateral output the present built-in quasi-optical mode converter consists of a launcher with feed waveguide deformation and three beam shaping mirrors. The helically cut launcher radiates the RF power via its straight cut onto the first phase correcting mirror of quasi-parabolic shape. The power reflected from the first mirror propagates as an astigmatic beam onto a series of two elliptical or hyperbolic reflectors where the astigmatism is removed and the output beam transverse dimensions are matched to the window size.

To achieve a sidelobe-free fundamental Gaussian beam as an output mode, the launcher must have feed waveguide deformations such that the incident rotating mode $TE_{28,8}$- is converted to a mode mixture generating a Gaussian beam distribution. To achieve such mode mixtures two methods have been established, the first, known as the Denisov [9,10] method and a second geometric optical (g.o.) based design principle that was first proposed in [11]. Since the first method is well known only the second

one will be described here.

The waveguide can be considered to be a transmission line of joined mirrors of parallelogram shape with axial length L_c and transverse width $\phi_c R_c$ defined by:

$$L_c = 2\pi R_w \frac{k_{//}}{k_\perp} \frac{\sqrt{1-\frac{m^2}{\chi_{mp}^2}}}{\cos^{-1}(\frac{m}{\chi_{mp}})} \tag{13}$$

$$\varphi_c = 2\cos^{-1}(\frac{m}{\chi_{mp}}) \tag{14}$$

$$R_c = \frac{m}{\chi_{mp}} R_w \tag{15}$$

To reduce diffraction effects the field at the mirror edges must be low compared to the field at the mirror center, more precisely, a quasi-Gaussian or raised cosine distribution with its maximum at the mirror center is desirable. According to [12] the optimum mode mixture can be calculated by means of a least squares fit.

In the transverse plane of the waveguide the principle of the g.o. based design method is described by means of Fig. 13(a), where the rays are incident from an initial circular caustic U with the radius R_c. This assumption is valid as long as the deformation of the waveguide is weak. The reflected rays from the first mirror propagate via an intermediate caustic V to the second mirror which reflects them into the final caustic W. To keep the amplitude of the deformations small, the final caustic is chosen to be circular at almost the same location as would be in the unperturbed case. However, by means of these two mirrors the density of the rays along the caustic is transformed from initially uniform to Gaussian-like. The general idea to achieve this change of amplitude density is to take advantage of two subsequent phase variations leading to an amplitude alteration. The main difference between this approach and the Denisov principle is that the size of the converting section is small enough that modes do not establish themselves which would only occur after they have propagated at least the Fresnel length. This results in a smaller length of the deformed feed waveguide for the g.o. approach compared to the Denisov principle. In the axial direction the same design procedure as for the azimuthal direction is performed. To distinguish the joined mirrors from the three quasi-optical mirrors in the subsequent text they will be called "in-waveguide-mirrors" or "segments".

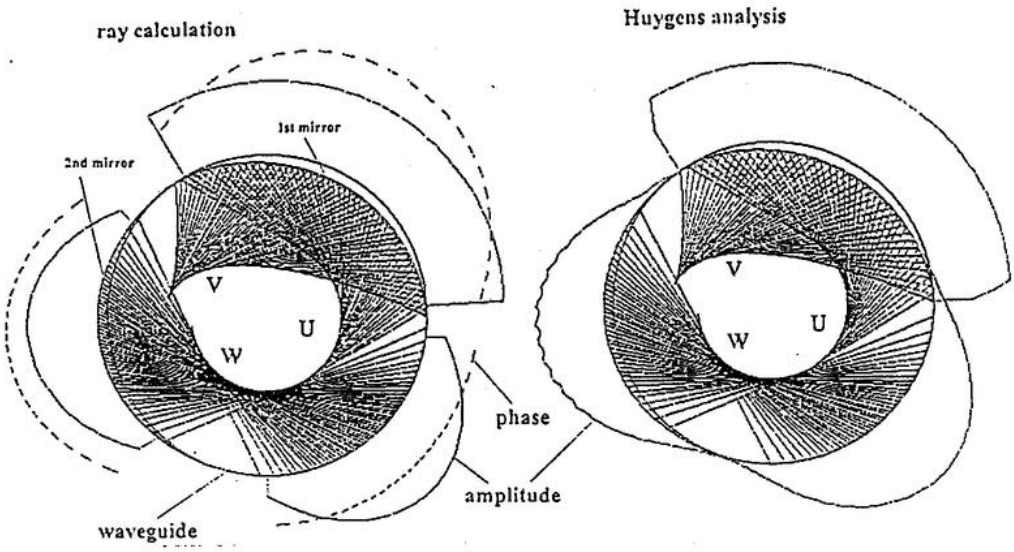

Fig. 13: Cross section of the launcher feed waveguide with two in-waveguide mirrors (azimuthal bunching), caustics amplitude distributions(-) and phase distributions(---) (a) geometrical optics (b) diffraction optics.

The waveguide perturbations synthesized by means of geometrical optics must be analyzed using diffraction theory. The calculation is separated in axial and azimuthal directions and the Huygens integrals are solved on surfaces depending on two dimensions. In this approach it is assumed that the field is radiated from a single caustic and it is calculated on the waveguide surface by means of Hankel functions. To obtain the radiation field of the launcher, the reflected field from the last waveguide mirror surface is computed and shown in Fig. 13(b).

Figure 14 shows the different lengths of the converter sections designed by the two different principles. It can be seen that the g.o. calculated converter is considerably shorter than the Denisov-type converter.

Also maximum wall losses have been calculated by means of two different methods, which agree to within *3%*. One method uses textbook formulas for waveguide attenuation for a mode mixture, while the second calculates the attenuation by means of the joined mirror consideration. The ohmic losses are depicted at specific points on the curves for different launcher lengths. Consideration of ohmic losses also predicts an advantage of the shorter g.o. calculated principle compared with the Denisov principle. However it should be mentioned that for lower-order modes the Denisov principle can be of advantage in comparison to the g.o. calculated principle.

The launcher with feed waveguide deformations has preliminary parameters and design constraints of *395mm* for the axial position of the cavity, *70mm* for the length of the uptaper, and *3mm* for the minimum allowable distance between the electron beam and the waveguide wall.

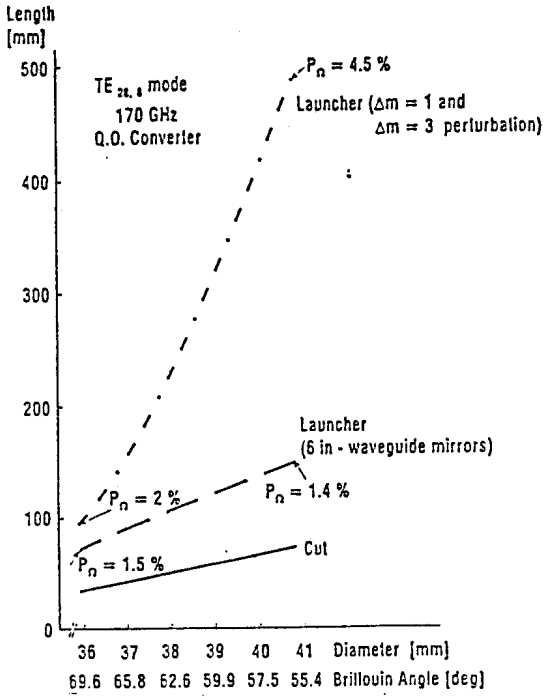

Fig. 14: Calculated length of mode converters operating on different principles vs. waveguide diameter. The ohmic losses are indicated at several points.

Considering these values and the electron beam path, a maximum launcher length is calculated to be *~200mm*. The optimum launcher radius can be determined as $R_W = 20mm$. For the design mode $TE_{28,8}$ the following parameters are obtained: Brillouin angle, $\theta_B = 57.5°$, caustic radius $R_c = 9.32mm$, segment heigth $L_s = 22.5mm$, cut length $L_c = 65.2mm$, overall length $L_{tot} = 200.4mm$, and length to the center ray $L_{cr} = 167.9mm$. The location of the center ray origin will have the coordinates: *(0mm, 9.32mm, 645mm)*. The reflection of RF power back into the launcher is computed with the MAFIA code to be less than *-40dB*.

Three mirrors, one phase correcting quasi-parabolic mirror used to flatten the curved phase front at the launcher aperture, and two elliptical or hyperbolic mirrors used to remove astigmatism, are required. The quasi-parabolic mirror can be calculated by means of standard formulas, however here it is tilted such that for the reflected center ray the transverse offset in the y-direction of the size R_c is removed. To avoid intersection of the RF beam by the launcher edge the mirror is placed three times the waveguide radius from the gyrotron axis. The position of the intersection of the center ray with the surface of the first mirror is determined to be: $P_{3Q} = (-60mm, 0mm, 683.2mm)$. At this point the location of the waist in the transverse direction (x-y or Q-plane) is located. Since this mirror is flat in the z-direction the waist in the x-z plane (or P-plane) is located at the

point P_{3P} = *(-120mm, 0mm, 645mm)*. The waist sizes are determined by the aperture of the deformed feed waveguide to be: waist in P-plane *18mm* and waist in Q-plane *25mm*. The non-astigmatic lateral output beam has its waist located at P_1 = *(-400mm, 0mm, 930mm)* and size of *25mm*.

These requirements and the constraints given by the electron beam lead to the final design. The overall system can be seen in Fig. 15. The computed overall mode purity of the Gaussian beam output is *96%*.

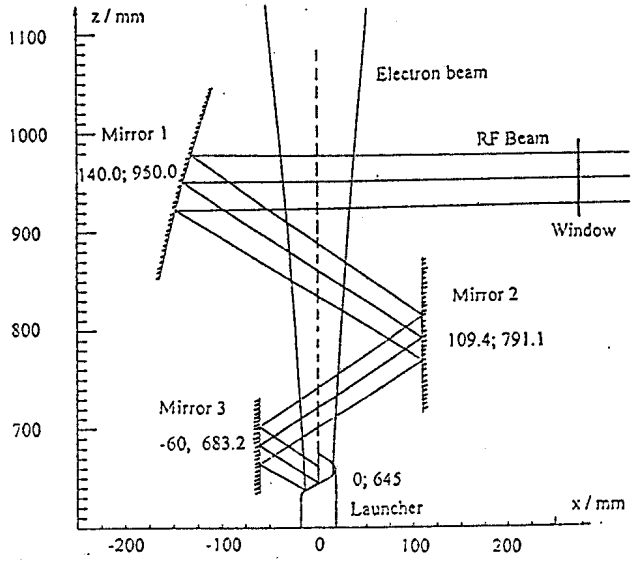

Fig. 15: Schematic in the x-z plane of the overall system depicting the launcher, the x-z profile of the external mirrors and the trajectories of the electron beam as well as the RF output beam.

6. GYROTRON WINDOW

From the viewpoint of the realization of *1MW CW* operation, essentially all components of present-day gyrotrons have been developed with the exception of the output window. At present, edge-cooled single-disc windows as well as surface-cooled double disc windows are in use, and cryogenically edge-cooled single disc sapphire windows as well as distributed windows are under test. The state-of-the-art is summarized in Table 4.

In the case of monochromatic radiation, wave reflections from the window are usually eliminated by one of the two methods: (a) a single periphery-cooled disc is used having a thickness of a multiple of the half-wavelength in the dielectric and (b) two of such resonant discs are combined to a double-disc window (with surface cooling) in which the distance between the two discs is tunable. As can be seen from Table 4, no windows for *CW* applications at the *MW* power level exist. To reach this goal, further developments of cryo-cooled sapphire windows are

underway at several labs (CEA Cadarache, FZK Karlsruhe, IAP Nizhny Novgorod, JAERI Naka, Thomson Vélizy, Toshiba Nasushiobara). In these designs, the extremely low absorption and the high thermal conductivity of pure sapphire in the temperature range between *20K* and *77K* will be utilized [13-16]. It should be mentioned that in the case of gyrotron windows eventual "cryopumping" of a cryogenic window appears to be no problem. The water cooled distributed window, that could also be used as torus window, is being developed at GA San Diego [17].

Material	Type	Power (kW)	Frequency (GHz)	Pulse Length (s)	Institution
alumina	single disk water edge cooled	200	60	0.1	VARIAN
water-free fused silica	single disk water edge cooled	200	60	5.0	UKAEA/Culham
boron nitride	single disk water edge cooled	600 550	140 140	2.0 3.0	SALUT TORIY
sapphire	single disk LN_2 edge cooled	285* 500 370	140 140 140	3.0 0.5 1.3	IAP/INFK FZK/IAP/IPF/IPP FZK/IAP/IPF/IPP
sapphire	single disk with Cu anchor LHe edge cooled	410	110	1.0	JAERI/TOSHIBA
sapphire	double disk FC75 face cooled	500 350 200	110 110 140	2.5 5.0 CW	VARIAN JAERI/TOSHIBA VARIAN
sapphire	distributed water cooled	65**	110	0.3	GA/JAERI/ TOSHIBA

Power densities required for 1 MW-level (*) and 0.8 MW-level (**) gyrotrons (HE_{11})

Table 4: Experimental parameters of high-power millimeter-wave vacuum windows.

6.1 Liquid Nitrogen Cooled Sapphire Window (T = 77K)

The theoretical limits for *CW* transmission of a circular (*D = 90mm*), single-disc, LN_2 sapphire window are summarized in Table 5 for different power density distributions at *140GHz*, *170GHz* and *220GHz*. The finite element calculations have been conducted using a power absorption factor $tan\delta = 3.15 \cdot 10^{-12}(T/K)^{3.3}$ (for Ti-doped sapphire at *140GHz*) together with the best value of thermal conductivity given by Touloukian (highest purity) [18]. Various experiments were performed to verify the design calculations. Heat transfer measurements were carried out with an electrically heated and well instrumented copper simulator and an original sapphire window in which the feasibility of the

chosen concept was demonstrated and the design calculations were verified [19]. By atmospheric evaporative cooling in liquid nitrogen, up to *1300W* can be safely removed at the edge of the window. This means that it is not the heat removal at the edge which limits the power transmittance of the window, but the radial removal of the heat absorbed in the window itself which already at *200W* to *300W* causes so-called thermal runaway. The use of a flattened elliptical Gaussian beam with an aspect ratio *8:1* transmitted through a rectangular window with corresponding aspect ratio increases the power capability at *170GHz* from *0.6MW* to *1MW*.

	140GHz	170GHz	220GHz
Gaussian profile (G)	0.5MW	0.4MW	0.3MW
flattened profile (F)	0.7MW	0.6MW	0.45MW
annular profile (A)	1.0MW	0.85MW	0.65MW

Table 5: Maximum power transmittance of a single disc, LN_2 edge-cooled sapphire window with resonant thickness (*5λ/2* at *140GHz*, *6λ/2* at *170GHz*, *8λ/2* at *220GHz*) for different power distributions.

6.2 Cryogenic Sapphire Window at T = 20-30K

Lowering the window temperature to $T = 20\text{-}30K$ results in a dramatic reduction of $tan\delta$ (Fig. 16) and allows to work in the range where the thermal conductivity of sapphire has its maximum (Fig. 17).

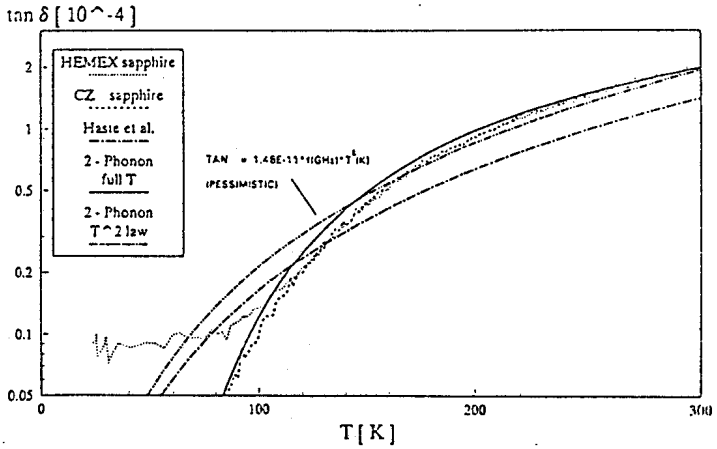

Fig. 16: Experimental loss data for sapphire (ordinary ray) at cryogenic temperatures and at *145GHz* and the description by model functions [20].

For heat removal one can use forced He-gas flow or in much simpler configurations a liquid helium cooled thermal copper anchor around the window disc [14]. Cooling down tests indicate that the cooling capacity is larger as the temperature of the window is higher and the deposited energy is smaller. A capacity of about *2W* and *10W* was obtained at a disc temperature of *20K* and *40K*, respectively. From a comparison with the calculated RF power deposition it is expected that an operation of three

minutes with *1MW* transmission power is feasible for this cryogenic window. In initial high power tests the operation of the window up to about *400kW* for *1s* pulses has been demonstrated. However the geometry of the thermal anchor must be improved in order to increase the maximum achievable heat removal.

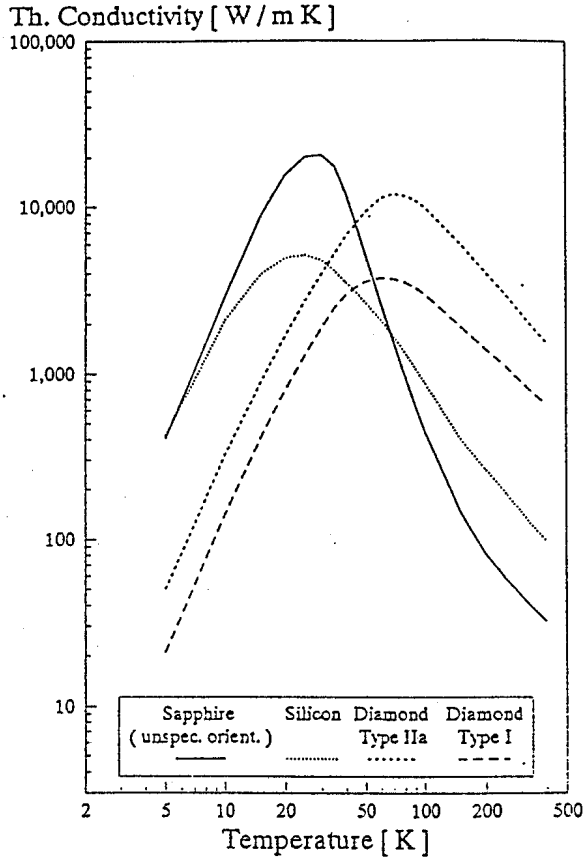

Fig. 17: Thermal conductivity ($Wm^{-1}K^{-1}$) recommended by Touloukian *et al* [18].

The use of a liquid neon bath at atmospheric pressure (*27.15K*) instead of the copper anchor simplifies the heat removal. Neon could be liquefied by making use of a flow of cold He gas. Since the gyrotrons will be far away from the ITER torus there is no danger of activation of the neon by fusion neutrons. Figure 18 plots the maximum *CW* transmission power (Gaussian beam/HE_{11}) for Ti-doped sapphire. This calculation was performed at FZK Karlsruhe assuming $tan\delta = 1.48 \cdot 10^{-11} \cdot (f/GHz) \cdot (T/K)^2$ (pessimistic value, see Fig. 16) and a relatively low value for the thermal conductivity recently measured at CEA Cadarache for HEMEX quality. One can easily see that the power transmission limit of a resonant window with a thickness of approximately *1.75mm* is *2.8MW*, *2.3MW*, and *1.8MW* at *140GHz*, *170GHz*, and *220GHz*, respectively.

6.3 Distributed Window

A novel vacuum window has been developed at General Atomics which uses a planar slotted structure of alternating thin sapphire bars with micro-channel water-cooled niobium hexagonal tubes [17]. Analysis indicates that a window *100mm* x *100mm* in area can carry *1MW* in the HE_{11} mode at *110GHz* and *1MW* with an appropriate HE_{11}/HE_{12} mode mixture at *170GHz*.

6.4 Alternative Window Materials

As a potentially new material for non-cryogenically cooled gyrotron windows, diamond is attractive due to its phenomenal tensile strength, modest dielectric constant, low loss and high thermal conductivity (Fig. 17). However present day chemical-vapor-deposition (CVD) capabilities have not yielded sufficiently thick samples with the required window diameter and the corresponding $tan\delta$-values are not low enough (Fig. 18). Current capabilities have allowed for tests with samples of *2.5cm* diameter and $\lambda/2$ thickness at $f = 145GHz$. The experimental $tan\delta$-values are shown in Fig. 18 [21].

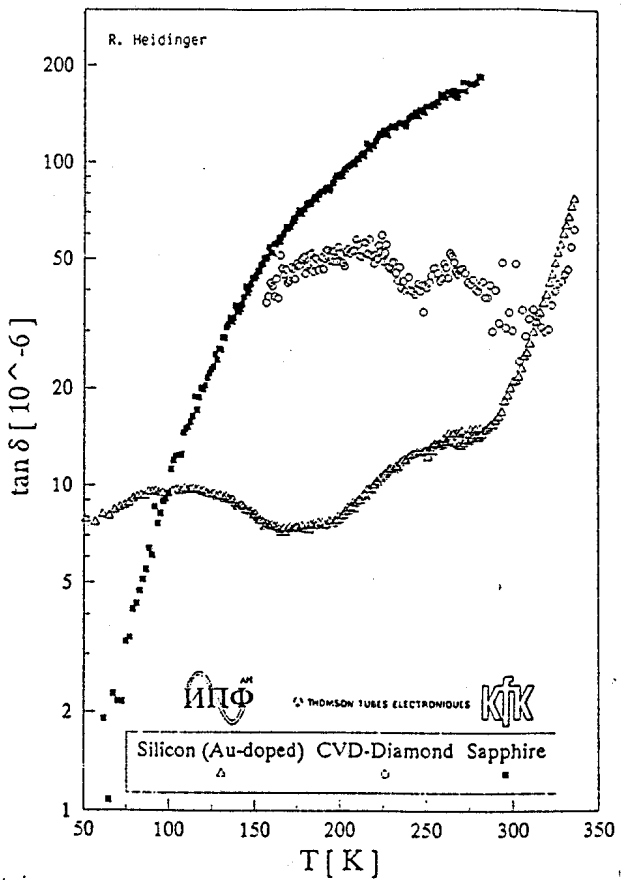

Fig. 18: Loss tangent as a function of temperature for low-loss window materials.

Another potential window material, an optimized silicon grade, is presently under investigation. For this material in the temperature range above *120K* the loss tangent is lower (Fig. 18) and the thermal conductivity is *3-4* times higher than that of sapphire (Fig. 16). Above *120K* the power carrying capability of a silicon window will exceed that of a comparable sapphire window. However it also can be deduced from Figs. 16 and 18 that at room temperature neither the loss tangent nor the thermal conductivity of the silicon material can reach the value of sapphire at *77K*. Thus it seems unlikely that the silicon material can be used for *MW CW* windows at room temperature. The temperature range around *180K* seems to be optimum for a silica window.

6.5 Options for *1MW CW 170GHz* gyrotron windows

In conclusion of this section on *mm*-wave vacuum windows, Table 6 summarizes possible options for *1MW CW 170GHz* operation. Options 3 and 4 are also well suited for use as a torus window.

	Material	Type	RF-Profile	Cross-Section	Cooling
①	Sapphire	single disk	flattened Gaussian	rectangular (285 mm x 35 mm)	LN_2 edge cooled (77 K) $\tan\delta = 6.7 \cdot 10^{-6}$, k = 1000 W/mK
②	Sapphire	single disk	Gaussian	circular (Ø = 100 mm)	LNe or LHe edge cooled (27 K) $\tan\delta = 1.9 \cdot 10^{-6}$, k = 2000 W/mK
③	Sapphire/Metal	distributed	flattened Gaussian	rectangular (100 mm x 100 mm)	internally water cooled (300 K) $\tan\delta = 2.5 \cdot 10^{-4}$, k = 40 W/mK
④	Diamond	single-disk	Gaussian flattened Gaussian	rectangular (200 mm x 50 mm) circular (Ø = 100 mm)	water edge cooled (300 K) $\tan\delta = 3.5 \cdot 10^{-4}$, k = 2000 W/mK
⑤	Silicon Au-doped	single-disk	flattened Gaussian	rectangular (300 mm x 34 mm)	edge cooled (200 K), cryo-cooler $\tan\delta = 8 \cdot 10^{-4}$, k = 250 W/mK

Table 6: Options for *170GHz 1MW CW* gyrotron window.

ACKNOWLEDGMENTS

We acknowledge fruitful discussions with Drs. P. Garin and H. G. Mathews of Thomson Tubes Electroniques and Dr. R. Heidinger of FZK Karlsruhe. This work was performed in the framework of the ITER sub-task IVA-I. It was partially supported by the project Kernfusion of the Forschungszentrum Karlsruhe, the Swiss National Science Foundation, and the EURATOM Fusion Programme. One of the authors (C. T. Iatrou) acknowledges the support received by the European Union programme Human Capital and Mobility.

REFERENCES

[1] R. Gruber, S. Merazzi, and T. M. Tran, "DAPHNE: A programming environment for gyrotron optimization", *16th Int. Conf. on Infrared and Millimeter Waves*, Lausanne, Switzerland, 1991, Conf. Digest **SPIE 1576**, pp. 122-124.

[2] A. Sh. Fix, V. A. Flyagin, A. L. Goldenberg, V. I. Khizhnyak, S. A. Malygin, Sh. E. Tsimring, and V. E. Zapevalov, "The problem of increase in power, efficiency and frequency of gyrotrons for plasma investigations", *International Journal of Electronics*, **57**, pp. 821-826, 1984.

[3] T. V. Borodachyova, A. L. Goldenberg, and V. N. Manuilov, "On recuperation in gyrotron", in *Gyrotrons*, V. A. Flyagin ed. (in Russian), pp. 161-180, 1989.

[4] M. E. Read, A. J. Dudas, W. Lawson, and A. Singh, "Depressed collectors for gyrotrons", *13th Int. Conf. on Infrared and Millimeter Waves*, Honolulu, Hawaii, 1988, Conf. Digest **SPIE 1039**, pp. 181-182.

[5] K. E. Kreischer, B. G. Danly, J. B. Schutkeker, and R. J. Temkin, "The Design of Megawatt Gyrotrons", *IEEE Transactions on Plasma Science*, **PS-13**, pp. 364-373, 1985.

[6] B. G. Danly and R. J. Temkin, "Generalized nonlinear harmonic gyrotron", *Physics of Fluids*, **29**, pp. 561-567, 1986.

[7] E. Borie, "Self consistent code for a 150GHz gyrotron", *International Journal of Electronics*, **72**, pp. 1079-1091, 1992.

[8] B. Jödicke, "Zur Modenrangigkeit von Hochleistungsgyrotrons mit Rotationssymmetrischen Arbeitsmoden", KfK Report 4603, Dec. 1989 and Ph.D. Thesis, University of Karlsruhe, 1988.

[9] G. G. Denisov, A. N. Kuftin, V. I. Malygin, N. P. Venediktov, D. V. Vinogradov, and V. E. Zapevalov, "110GHz gyrotron with built-in high efficiency converter", *International Journal of Electronics*, **72**, pp. 1079-1091, 1992.

[10] G. G. Denisov, M. I. Petelin, and D. V. Vinogradov, "Effective conversion of high waveguide modes to eigenmodes of open mirror lines", Proc. Xth School-Seminar on Wave Diffraction and Propagation, Moscow, SRIRP, pp. 96-128, 1993.

[11] A. Möbius and J. Pretterebner, "Avoidance of edge diffraction effects of WGM-fed quasi-optical antennas by feed waveguide deformation", *16th Int. Conf. on Infrared and Millimeter Waves*, Lausanne, Switzerland, 1991, Conf. Digest **SPIE 1576**, pp 531-532.

[12] J. Pretterebner, A. Möbius, and M. Thumm, "Improvement of quasi-optical mode converters by launching an appropriate mixture of modes", *17th Int. Conf. on Infrared and Millimeter Waves*, Pasadena, USA, 1992, Conf. Digest **SPIE 1929**, pp. 40-41.

[13] H. E. Häfner, E. Bojarsky, P. Norajitra, and H. Reiser, "Cryocooled windows for high frequency plasma heating", *Proc. 7th*

Symposium on Fusion Technology, Rome, Italy, 1992, eds. C. Ferro, M. Gasparotto, H. Knoepfel (Elsevier Science Publishers B.V. 1992), pp. 520-523.

[14] Y. Saitoh, K. Itoh, T. Yoshiyuki, K. Ebisawa, K. Yokokura, T. Nagashima, and T. Yamamoto, "Cryogenic window for millimeter-wave transmission", *Proc. 7th Symposium on Fusion Technology*, Rome, Italy, 1992, eds. C. Ferro, M. Gasparotto, H. Knoepfel (Elsevier Science Publishers B.V. 1992), pp. 632-636.

[15] M. Pain, G. Berger-By, J. J. Capitain, J. P. Crenn, F. Smits, and G. Tonon, "The 110GHz electron cyclotron heating and current drive system of Tore Supra", *Proc. 8th Joint Workshop on Electron Cyclotron Emission and Electron Cyclotron Resonance Heating (EC-8)*, Gut Ising, Germany, 1992, Vol. II, pp. 523-530.

[16] A. S. Fix and P. B. Sushilin, "RF windows for gyrotrons and tokamaks: A way to 1MW/CW", *Proc. 2nd Int. Workshop on Strong Microwaves in Plasmas*, Nizhny Novgorod, 1993, Paper S48.

[17] C. P. Moeller, J. L. Doane, and M. DiMartino, "A vacuum window for a *1MW CW 110GHz* gyrotron", *19th Int. Conf. on Infrared and Millimeter Waves*, Sendai, Japan, 1994, Conf. Digest JSAP AP 941228, pp. 279-280.

[18] Y. S. Touloukian, R. W. Powell, C. Y. Ho, and P. G. Klemens, "*Thermal physical properties of matter*", New York: IFI Plenum, 1970.

[19] H. E. Häfner, E. Bojarsky, K. Heckert, P. Norajitra, and H. Reiser, "Liquid nitrogen cooled window for high frequency plasma heating", *Journal of Nuclear Materials*, 212-215, pp. 1035-1038, 1994.

[20] G. Link and R. Heidinger, "Modelling of intrinsic mm-wave absorption in low loss dielectrics with complex crystal structure", *18th Int. Conf. on Infrared and Millimeter Waves*, Colchester, UK, 1993, Conf. Digest SPIE 2104, pp. 150-151.

[21] R. Heidinger, "Dielectric property measurements on CVD diamond grades for advanced gyrotron windows", *19th Int. Conf. on Infrared and Millimeter Waves*, Sendai, Japan, 1994, Conf. Digest JSAP AP 941228, pp. 277-278.